Rayleigh lidar system for middle atmosphere research in the arctic

Jeffrey P. Thayer
Norman B. Nielsen
Russell E. Warren
Craig J. Heinselman
SRI International
3333 Ravenswood Avenue
Menlo Park, California 94025
E-mail: jeff_thayer@qm.sri.com

Jens Sohn
Danish Meteorological Institute
Kellyville Radar
Postboks 108
3910 Kangerlussuaq
Greenland, Denmark

Abstract. A Rayleigh/Mie lidar system deployed at the Sondrestrom Atmospheric Research Facility located on the west coast of Greenland near the town of Kangerlussuaq (67.0 deg N, 50.9 deg W) has been in operation since 1993 making unique observations of the arctic middle atmosphere. The vertically directed lidar samples the elastically backscattered laser energy from molecules (Rayleigh) and aerosols (Mie) over the altitude range from 15 to 90 km at high spatial resolution. The limited amount of arctic observations of the middle atmosphere currently available emphasizes the importance and utility of a permanent Rayleigh lidar system in Greenland. The lidar system consists of a frequency-doubled, 17-W Nd:YAG laser at 532 nm, a 92 cm Newtonian telescope, and a two-channel photon counting receiver. The principal objective of the lidar project is to contribute to studies concerned with the climatology and phenomenology of the arctic middle atmosphere. To this end, we describe the lidar system in detail, evaluate system performance, describe data analysis, and discuss the system capabilities in determining the density, temperature, and the presence of aerosols in the arctic middle atmosphere. Particular emphasis is placed on the derivation of temperature from the lidar measurement and on the impact of signal-induced noise on this analysis. Also, we develop a statistical filter based on a Bayesian approach to optimally smooth the lidar profile in range. This filter preserves the short-term fluctuations in the low-altitude data consisting of relatively high SNR, whereas more smoothing is applied to the high-altitude data as the SNR decreases. [S0091-3286(97)01607-3]

Subject terms: lidar; Rayleigh scatter; middle atmosphere; arctic; temperature; aerosols.

Paper 21096 received Sep. 14, 1996; revised manuscript received Feb. 3, 1997; accepted for publication Feb. 3, 1997.

1 Introduction

The middle atmosphere is a region of the earth's atmosphere that extends in altitude from approximately 15 to 100 km encompassing both the stratosphere and mesosphere regions. In the arctic, this region is host to many unique conditions and phenomena. For example, in the arctic summer, polar mesospheric clouds (or noctilucent clouds) near 83 km altitude form and appear to be increasing over time with possible linkages to increasing methane in the troposphere.[1] In the arctic winter, polar stratospheric clouds near 18 to 25 km form and have direct ties to stratospheric ozone destruction.[2] The arctic middle atmosphere is also where the intuitively contradictory observation of much colder temperatures in the summer than winter in the upper mesosphere occurs and illustrates the importance of dynamical forcing on the thermal balance in this region.[3] Another dynamic process in the arctic is the persistence of a strong polar stratospheric vortex in winter and the intermittent breakdown of this vortex creating dramatic warmings of the stratosphere and coolings of the mesosphere.[4] These phenomena may be linked to global processes but remain unique to the polar middle atmosphere. A useful means for studying many of these phenomena as well as providing synoptic and climatological data on the basic parameters of density, temperature, waves, and wind in the middle atmosphere is the lidar technique. Although there are many approaches to lidar, in this paper, we concentrate on what has become known as the Rayleigh lidar technique.

The Rayleigh lidar technique has proved to be an extremely valuable tool for studying the dynamic and thermodynamic properties of the middle atmosphere. Accurate measurements of the thermal structure in the middle atmosphere determined from Rayleigh lidar observations (e.g., Refs. 5 and 6) have become a routine monitoring capability for most systems. This capability of Rayleigh lidars has enabled detailed observations of stratospheric warming events[7] and has begun to contribute significantly to describing the climatological thermal structure in the arctic middle atmosphere. An anomolous feature of the middle atmosphere thermal structure that has recently been definitively confirmed by Rayleigh lidar observations is the mesosphere temperature inversion layer (e.g., Refs. 8 to 10). Investigations by Schmidlin,[11] Hauchecorne et al.,[8] Clancy and Rusch,[12] Hauchecorne and Maillard,[13] Meriwether et al.,[9] and Whiteway et al.[10] have characterized the layer as a temperature enhancement in the upper mesosphere in excess of 10 K over model profiles (Meriwether et al.,[9] observed temperature enhancements as large as 50 to 100 K) with a thickness of 10 km in altitude and whose peak altitude is seasonally dependent. These inversion layers have been reported by Rayleigh lidar stations of subarctic latitudes, while arctic observations have not been as conclusive about the presence of these layers. Arctic observations of middle atmosphere temperature structure have been characterized as very stable with little deviation in the summer,[14] while winter profiles are more dynamic due to large-scale wave propagation.[15]

Rayleigh lidar measurements of the background molecular number density and the perturbations about that background field have contributed significantly to gravity wave studies in the middle atmosphere (e.g., Refs. 7 and 16 to 24). Except for Whiteway and Carswell,[7] these studies were made by lidar facilities at subarctic latitudes. Whiteway and Carswell combined the thermal and gravity wave measurements derived from a Rayleigh lidar in Eureka, Northwest Territory, Canada (80 deg N, 86 deg W), to investigate the gravity wave transmission during a stratospheric warming. They found substantially greater gravity wave dissipation occurred during the event than occurred before and after the warming. Semidiurnal and diurnal tidal influences on the middle atmosphere have also been observed in Rayleigh lidar density measurements (e.g., Ref. 25), illustrating similar tidal behavior as found by rocket and radar studies. Wind measurements by Doppler Rayleigh lidars (e.g., Refs. 26 and 27) of the mean wind field in the middle atmosphere offer a unique capability for studying wave-mean flow interactions on a routine basis.

The ability of Rayleigh lidar to determine the vertical distribution of aerosol backscatter has led to important contributions to studies concerned with aerosol and cloud effects on climatic processes. One particular research area benefiting from Rayleigh lidar measurements is the study of noctilucent clouds (e.g., Refs. 14, and 28 to 32). These ground-based lidar observations have provided detailed and accurate measurements of the cloud's height, thickness, vertical structure, backscatter ratio, surrounding temperature structure, and temporal evolution that would, otherwise, be accessible only by rocket. Studies of polar stratospheric clouds and volcanic aerosols, most recently due to the effects of the Mt. Pinatubo eruption, have also benefited greatly by the Rayleigh lidar technique.

In the winter of 1992 to 1993, a Rayleigh lidar system was installed at the established NSF Sondrestrom Research Facility located on the west coast of Greenland near the town of Kangerlussuaq (67.0 deg N, 50.9 deg W). The principal objective of the Rayleigh lidar is arctic middle atmosphere research, involving the topics already discussed, and coupling of the middle atmosphere with the upper atmosphere, although lower atmosphere research is also of interest. It has only been within the past couple of years that Rayleigh lidars capable of accurate monitoring of the middle atmosphere have been permanently established in the arctic: these systems include the Arctic Lidar Technology (ARCLITE) facility in Greenland (67 deg N, 50 deg W), described in this paper; the ALOMAR observatory near Andoya, Norway (69 deg N, 16 deg E), established[33] in 1994; and the ASTRO observatory near Eureka, Northwest Territory, Canada, established[34] in 1993. The limited amount of high-latitude observations of the middle atmosphere currently available emphasizes the importance and utility of a permanent lidar system in Greenland to investigate properly the phenomenological, synoptic, and climatological properties of the arctic middle atmosphere on a continuous, long-term basis. These lidar measurements have already begun to contribute significantly to polar middle atmosphere research, with unique measurements of noctilucent clouds in the summers of 1994 (Ref. 32) to 1996.

This paper discusses and describes the lidar system in detail; evaluates system performance; describes data analysis and signal processing; and discusses the system capabilities in determining the density, temperature, and aerosol presence in the arctic middle atmosphere. A unique approach to processing the lidar data is presented where we apply a Bayesian approach to the signal statistics to develop a statistically based filter for the data. Also, a detailed discussion of the temperature analysis is presented concerning the effects of signal-induced noise on the derived temperature. Although capable of deriving gravity wave parameters from the lidar signal, the gravity wave analysis will be presented in a subsequent paper.

2 Instrument Description

Since 1983 the NSF Sondrestrom Atmospheric Research Facility in Greenland has been making observations of the earth's atmosphere using optical and rf instrumentation. During that time, both active and passive remote-sensing instrumentation have been operated at the site. These collocated, multisensor observations have been used to investigate the arctic regions of the atmosphere from the troposphere to the magnetosphere. The installation of the vertically directed lidar system, called the ARCLITE facility, in the winter of 1992 to 1993 enhances the research base of the site for middle and lower atmosphere research by sampling the elastically backscattered laser energy from molecules (Rayleigh) and aerosols (Mie) over the altitude range from 15 to 90 km at high spatial resolution. The impressive assemblage of optical and rf instrumentation at the site invites many new collaborative, multi-instrumented experiments to be carried out with the lidar.

The requirements of high spatial and temporal resolution and good signal statistics for middle atmosphere research prescribe certain specifications for Rayleigh lidar systems. These specifications include high-energy, high-repetition lasers, narrow laser beam divergences, narrow laser linewidths, laser wavelengths that provide high atmospheric transmittance with strong Rayleigh backscatter properties, large-aperture telescopes with submilliradian fields of view, narrow spectral passbands, and maximized optical throughput. These factors have been incorporated into the design of the ARCLITE system. Figure 1 is an illustration of the ARCLITE system layout showing the main components of the system. The following paragraphs describe the system layout in more detail; refer to Fig. 1 throughout this discussion. Table 1 lists the specifications of the main components of the lidar system.

The lidar system employs a monostatic configuration with the transmitter and receiver in a biaxial arrangement at a separation distance of 1 m. Due to the harsh arctic environment, a roof hatch and window system (not shown in Fig. 1) was designed for the lidar with the laser transmitting through a chimney in the roof and the telescope environ-

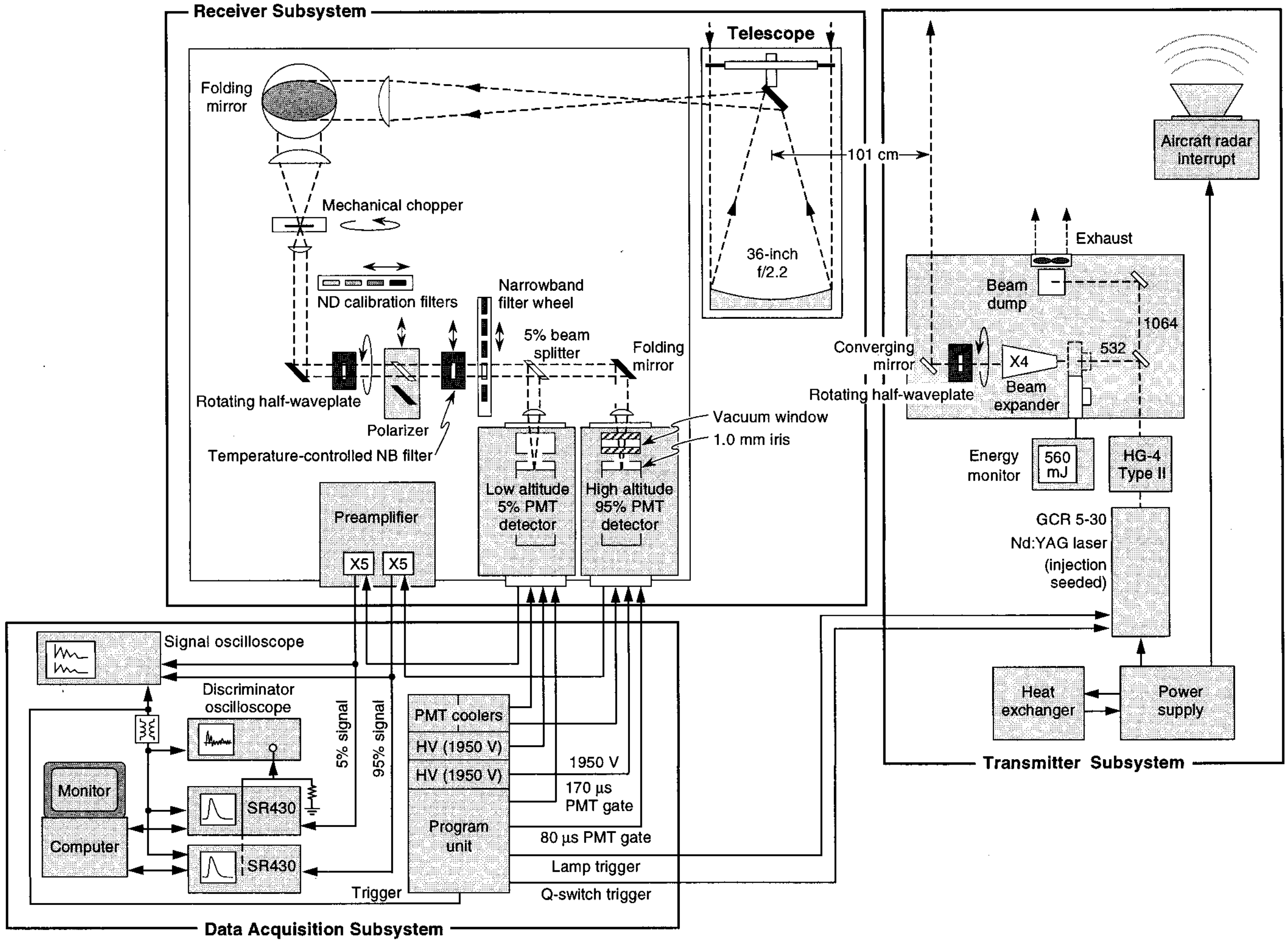

Fig. 1 ARCLITE system configuration.

mentally protected by a window made of B-270 water-white crown glass with 92% transmission at 532 nm.

The ARCLITE transmitter is the 42-W Spectra-Physics Nd:YAG laser, model GCR 5-30, with injection seeding and a second harmonic generator for partial conversion to 532.0 nm. The frequency-doubled laser pulses are transmitted into the atmosphere after dichroic separation from the 1064 nm pulses and passage through a (×4) beam expander to reduce the divergence in the laser beam to less than 0.1 mrad. Prior to a night of observations, the 532 nm pulse energy is examined by an energy monitor and the reading is recorded; pulse energies of 560 mJ at 30 Hz PRF are typical. With injection seeding, the laser linewidth is

Table 1 ARCLITE system specifications.

Transmitter (Spectra-Physics GCR 5-30 Nd:YAG)		Receiver (Newtonian Telescope Configuration)		Signal Processing (Photon Counting Data Acquisition System)	
Wavelength	532 nm	Telescope diameter	92 cm	Data system	SR430
Pulse width	7 ns	Focal length	203 cm	Maximum count rate	100 MHz
Pulse repetition rate	30 Hz	Field of view	0.5 mrad	Range bin size	192 m
Pulse energy	560 mJ	Number of channels	2	Number of range bins	1024
Average power	17 W	Filter bandwidth		One-line integration	1 min
Seeded linewidth	105 MHz	Nighttime	1.0 nm	Computer system	PC 486-33
		Daytime	0.08 nm		
Beam divergence	0.1 mrad			PMTs (2)	EMI 9863B/100

significantly narrowed to near 0.0035 cm^{-1} (0.099 pm or 105 MHz) with no observed decrease in pulse energy. A 400 MHz oscilloscope, Tek 2467-B, with a fast refresh rate, is used to monitor the 10 ns transmitted pulses to ensure proper seeding of the laser. A laser mirror mount coaligned with the telescope optical axis is used to provide precise pointing of the laser beam for convergence of the transmitted beam within the field of view of the telescope.

The design and construction of the receiver system was centered around the Newtonian telescope, which consists of a 92 cm diameter, $f/2.2$ primary mirror. The receiver optics are mounted on the side of the telescope body to allow for accessibility and to enable the entire receiver to be tilted off vertical. The backscattered laser energy is collected by the telescope and collimated by an objective lens. The collimated light is then redirected by a folding mirror and focused onto the mechanical chopper mechanism. The chopper was recently installed due to the recognition of signal-induced noise present in our background signal; Section 4 discusses this effect further and Section 5 presents its impact on the temperature analysis. The mechanical chopper wheel consists of two blades on opposite sides and rotates at a rate of 220 Hz. The chopper blade position is monitored by a photodiode whose signal is used to trigger a pulse delay generator. After sufficient delay, the laser and data acquisition system are triggered. Presently, the chopper becomes fully open at an altitude of about 15 km.

Once the light passes through the mechanical chopper, it is collimated for transmission through an interference filter. The filters are contained within a filter wheel and include a 1.0 nm bandwidth filter centered on 532.0 nm with 57% transmission, a 1.0 nm bandwidth filter centered on 607.7 nm with 50% transmission, an open position, and a blocking position. The 532 nm filter is used for typical nighttime observations. The 607.7 nm filter allows for measurements of the N_2 Raman-shifted signal excited by the 532 nm laser energy. Other options in the receiver package include a set of neutral density filters for attenuation and calibration purposes, a half-wave plate and polarizer for transmission of linearly polarized light, and a 0.08 nm bandwidth temperature-controlled Daystar filter with about 25% transmission at 532.05 nm. The polarizer and the Daystar filter have their application during high background conditions. The telescope field of view is typically set to 0.5 mrad through the use of an iris in front of each of the photomultiplier tubes (PMTs).

Two thermoelectrically cooled PMTs (EMI 9863B/100—14 stage dynode structure) with S20 photocathodes and 2.5 mm apertures account for the large dynamic range introduced by the desired altitude coverage of the system. The return signal is separated by a beamsplitter with about 5% of the signal reflected into the first PMT and 95% of the signal transmitted to the second PMT. Owing to the birefringence of the beamsplitter, we can control somewhat the separation percentage of light between the two PMTs by rotating the half-wave plate, leaving the beamsplitter untouched. The quantum efficiencies for the PMTs are about 12% at 532 nm. Electronic gating circuits regulate the high voltage applied to the PMTs and act as an additional shutter for the PMTs.

The data acquisition system incorporates photon-counting electronics to record the incoming pulses from the PMTs in successive time bins. The output of a PMT is a current pulse that is then converted to a voltage pulse by a load resistor. The pulses generated by the PMTs are amplified (typically 5 to 25 times) by a 300 MHz preamplifier to bring the pulse voltages into an acceptable range for the multichannel scaler SR430, which combines amplifiers, discriminators, bin clocks, and data analysis in a single integrated instrument. The multichannel scaler provides gated sampling of the lidar signal with bin resolutions as high as 1 m and a count rate of 100 MHz.

To optimize the counting efficiency of the data acquisition units (SR430s) it is important to provide narrow pulses with sufficient amplitude to distinguish the signal pulses from background noise—that is, good pulse height distribution. To improve the shape of the PMT pulses, we employ a snubber circuit at the output of the PMT. The snubber consists of a 12-in. piece of coaxial cable and a potentiometer that effectively reduces ringing of the signal and sharpens the falling edge of the pulse by matching the PMT and transmission line impedances. This circuit allows for better resolution between individual pulses and, therefore, better counting accuracy by the SR430s. The pulse-pair resolution or count rate of the data acquisition electronics is typically the limiting factor for the time resolution of the entire photon counting system. The SR430 has a pulse-pair resolution of 10 ns; therefore, at high count rates discriminating between a single pulse and multiple fast pulses (the electronic equivalent to pulse pile-up) becomes an important issue.

The discriminator voltage setting is also an important system parameter that needs to be selected carefully. The discriminator optimizes the linear response of the PMT during high count rates and improves the signal statistics by setting the voltage above the noise pulse height but below the mean pulse height of the signal. The ARCLITE discriminator voltages for the two PMTs are first set by monitoring the PMT pulses on a fast oscilloscope and determining the voltage that is below the mean pulse height but above the noise level due to ringing, amplifier noise, or environmental noise. The discriminator voltages are then set for linearity using neutral density filters and applying the approach described by Donovan et al.[35] The discriminator voltage levels are sufficiently below the pulse height so that changes in the pulse height distribution due to gain changes or other effects will not result in count rate changes or drift.

At the request of the Danish government, we built a surveillance radar for synchronization with the laser to prevent laser illumination of aircraft. The radar uses a vertical horn antenna with a 12 deg beamwidth and 22 dB gain, an operating frequency of 9410 MHz with a pulse repetition rate of 800 Hz, and a peak power of 10 kW for detection of local as well as high-altitude aircraft. The laser is interlocked with the radar so that the Q-switch delay is temporarily interrupted and the laser shuts off when a target is detected within the 12 deg radar beam. Once out of the radar beam, the laser returns to normal operations automatically.

3 Signal Processing

During typical lidar operations, the laser is fired by a 30 Hz external trigger provided by the program unit (see Fig. 1).

The chopper and pulse delay generator provide the starting pulse for the program unit. The program unit then provides the trigger for the laser and the oscilloscopes monitoring the lidar return signal, and commands the SR430 units to start acquiring data. Typically, the SR430 units are set up to record the photon counts received by the two PMTs at a range resolution of 192 m and an on-line integration time of 1 min or 1800 shots. Because of the relatively low count rates, particularly for the high-altitude gates, both data averaging and altitude smoothing are required to infer useful profiles of atmospheric density and temperature. In addition to the on-line averaging provided by the 1-min integration of 1800 pulse returns, additional off-line averaging of the data can be used to reduce estimation variance at the cost of temporal resolution. However, extended averaging of many 1-min profiles has the disadvantage of (1) obscuring transient or time periodic events of physical significance and (2) introducing trends by mixing data belonging to different statistical populations—that is, nonstationary data. For these reasons it is useful to construct profile estimators that preserve the temporal resolution of the data inherent in the 1-min samples while optimally reducing the noise variance.

Performing optimal data smoothing requires a probabilistic model for the observed counts as a function of altitude and time. For high-altitude data having negligible signal content, the statistics are well described by a simple Poisson model parameterized by the mean background count $\langle b \rangle$. Figure 2(a) compares various probability density estimates for high-altitude (80 km) lidar data. The solid curve represents a histogram of the mean counts accumulated over 1-min integrations for a 2-h period of observations. The dotted curve represents a Gaussian or normal density function with the sample mean and sample variance computed from the lidar data using the expressions

$$\sigma_x^2(z) = \frac{1}{n-1} \sum_{t=1}^{n} [x(z,t) - \langle x(z) \rangle]^2, \tag{1}$$

and

$$\langle x(z) \rangle = \frac{1}{n} \sum_{t=1}^{n} x(z,t).$$

Here, n is the number of 1-min profiles integrated, z is the altitude index, and t is the time index. The dashed curve represents a Poisson density function with the variance equal to the mean of the counts. The close agreement of the curves in Fig. 2(a) demonstrates the expected Poisson behavior of the data at these high altitudes.

At lower altitudes for short integration periods, the accumulated lidar signal is again Poisson whose variance is the mean of the total counts $\langle x(z) \rangle$, consisting of mean signal and background counts $\langle s(z) \rangle + \langle b \rangle$, where $\langle s(z) \rangle$ denotes the mean signal counts collected at altitude z. For longer integration periods, however, the observed sample variance of the data $\sigma_x^2(z)$ in the signal bearing region is larger than that expected from the Poisson model result—that is, $\sigma_x^2(z) > \langle s(z) \rangle + \langle b \rangle$. An illustration of this behavior is shown in Fig. 2(b), which shows the same probability density estimates as in Fig. 2(a) but for the low-altitude data of 32 km. In this case, the normal probability density function models the observed counts very well, while the Poisson model is a much poorer fit and has a variance much smaller than that observed.

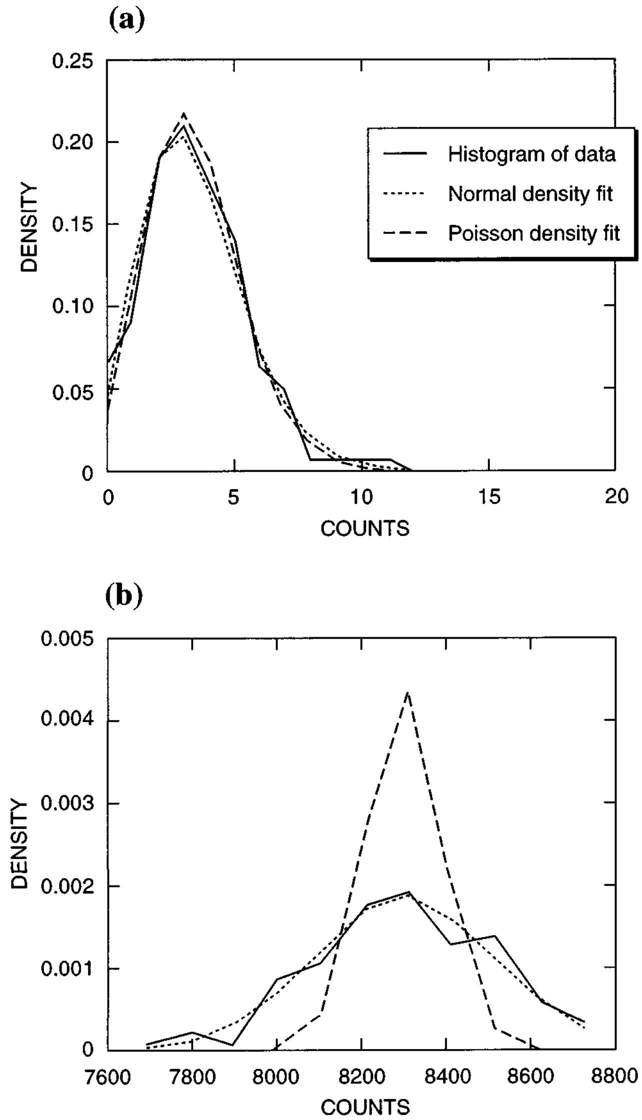

Fig. 2 Probability density estimates for (a) high-altitude (80 km) data and (b) low-altitude (32 km) data.

This additional variance is the result of variations in the backscattered signal due to changes in the atmospheric density within the postintegration period. Note that this additional variance should be distinguished from the possibility of trend indicated earlier; whereas the latter is caused by systematic long-term change in the underlying atmospheric density, the former is caused solely by the nature of the stationary random process under investigation. It is this additional non-Poisson component to the variance that characterizes the physical process we are attempting to estimate. Thus, the total sample variance expressed by Eq. (1) is equal to the mean counts plus the additional variance $\sigma_s^2(z)$ associated with the variability in the scattering medium—that is,

$$\sigma_x^2(z) = \langle x(z) \rangle + \sigma_s^2(z). \tag{2}$$

In fact, the variability in the scattering medium is caused by atmospheric internal gravity waves and, thus, the estimation of $\sigma_s^2(z)$ from the measurement allows for profiles of the root-mean-square (rms) perturbation and available potential energy density of gravity waves to be determined. These estimates can then be used to infer whether dissipation of wave energy is occurring over the altitude range[36] of 30 to about 55 km.

The ability to distinguish between the variance caused by the counting statistics and the natural variance of the scattering medium forms the basis for constructing a statistically based filter for removing as much of the Poisson counting fluctuations from the raw profiles as possible while preserving the fluctuations due to the density itself. This filtering approach has been used in differential absorption lidar (DIAL) measurements[37] with the filter having the form of a nonstationary Wiener filter that is applied to the signal $\langle s(z) \rangle$ to provide smoothed estimates $\hat{s}(z)$. In the appendix we outline the derivation of the statistical filter. The basic idea underlying the filter construction in the appendix is to use many 1-min profiles to estimate the parameters of a model for the expected variability of the signal process $s(z)$. In practice, that variability is specified by the mean signal counts and covariance matrix given below by Eqs. (3) and (5). The resulting signal model is used as the prior component in a Bayesian calculation of the estimated signal for each of the 1-min data records.

The Bayesian approach assumes that the parameter to be estimated is a realization of a random variable that is described by its probability density function (PDF). If some prior knowledge of the variable is available, then we can incorporate it into our estimator by determining the prior PDF. We have shown in Fig. 2 that a Guassian prior PDF is appropriate and tractable with the information gained by integrating data over long periods. By definition, a Bayesian estimate combines prior information with likelihood input derived from short-term data to produce a composite description of the signal. In this way, short-term fluctuations in the data are preserved for range gates having relatively high SNR, whereas more smoothing is applied to higher gate data for which the Poisson noise dominates the measurement. We note that use of long-term data to construct the prior signal model is only one possible approach, the use of physical models to derive prior estimates would be an interesting alternative.

Processing of the data using the filter requires the following steps:

1. On a per minute basis, estimate the sample mean background $\langle b(t) \rangle$ from many range gates in a region void of signal; in practice, these gates are chosen to lie at altitudes between 110 and 140 km.
2. Given a collection of 1-min profiles of raw count data, estimate the sample mean $\langle x(z) \rangle$ and sample variance $\sigma_x^2(z)$ given in Eq. (1). Using these results and those from step 1, the mean signal counts $\langle s(z) \rangle$ and the variance associated with the underlying physical processes are estimated as

$$\langle s(z) \rangle = \frac{1}{n} \sum_{t=1}^{n} [x(z,t) - \langle b(t) \rangle], \tag{3}$$

$$\sigma_s^2(z) = \sigma_x^2(z) - \langle x(z) \rangle. \tag{4}$$

3. The range gate covariance $\Lambda_s(z,z')$ is modeled and then computed as

$$\Lambda_s(z,z') = \sigma_s(z)\sigma_s(z')\exp\left[-\frac{(z-z')^2}{\gamma(z)^2}\right], \tag{5}$$

   using Eq. (4) and an estimate for the gate correlation scale parameter $\gamma(z)$. The values for $\gamma(z)$ are user-dependent and determine the degree of smoothing with altitude. This covariance model is an expedient that should in the future be replaced with sample measurements of the actual correlation structure. There is an altitude limitation in the determination of the variance of the scattering medium given in Eq. (4) as the Poisson error increases with height. Therefore, when estimating the gate covariance at high altitudes we use $\sigma_x^2(z)$ in place of $\sigma_s^2(z)$ in Eq. (5).
4. The estimates determined in steps 2 and 3 form the prior information necessary to construct the filter. These estimates are presently smoothed using a running average of 3 km width. From these estimates the smoothing kernels H are constructed using Eqs. (18) and (19) in the appendix.
5. The raw count data for each 1-min (or longer) integration period is then processed with the filter given by Eq. (18) in the appendix.

The filtered estimate of the signal is given as $\hat{s}(z)$ and, from Eq. (24) in the appendix, its variance may be approximately written as

$$\sigma_{\hat{s}}^2(z) = \frac{\langle x(z) \rangle}{1 + \langle x(z) \rangle / \sigma_s^2(z)}. \tag{6}$$

As shown in the next section, the variance in the scattering medium exceeds that described by a Poisson distribution for altitudes below about 55 km, resulting in little smoothing of the data and a filter variance similar to the Poisson estimate. As the Poisson error relative to the signal increases with altitude and exceeds the variance in the medium, smoothing of the data is performed by the filter and the variance of the estimate is reduced.

It should be noted that in estimating the rms error from these variance estimates, the variances should be divided by the n number of minutes or range cells accumulated in determining these estimates. It can be shown that this is equivalent, when Poisson statistics dominate, to the more typical approach of estimating the rms error by taking the square root of the total counts over so many accumulated minutes or range cells.

The following sections apply this filter algorithm to various data sets.

4 System Performance

The performance of a Rayleigh lidar system is largely determined by the product of the laser power and the telescope area. This power-aperture product, typically expressed in units of watts times square meters, can be used to compare the performance between lidar systems if all the other factors, such as the spatial and temporal resolution, atmospheric extinction, and optical efficiency are equivalent and the background noise is negligible (e.g., Ref. 38). Using the information given in Table 1, the power-aperture product for the ARCLITE system is 11.2 Wm^2. Although the power-aperture product provides a means to gauge other Rayleigh lidar systems, it is the statistical error of the measured lidar signal that provides an accurate evaluation of system performance. Ignoring systematic errors for the time being, the statistical error of the signal will be the limiting factor in determining how well parameters such as aerosol backscatter ratio, temperature, density, and wave characteristics can be derived from the lidar profile. The following discussion illustrates the system performance for the two cases of low and high background conditions based on the signal statistics discussed before and in Section 3.

4.1 *Low-Background, Nighttime Observations*

As Rayleigh lidar systems are noise-limited in altitude, nighttime observations accompanied with clear skies and low background noise are the best conditions for evaluating system performance. During these conditions only the 532 nm filter with 10 Å bandwidth is used in the ARCLITE receiver. Figure 3 contains plots from a sample of data taken during the night of April 10, 1996. Figure 3(a) is an illustration of raw lidar profiles from the high-altitude and low-altitude channels detected directly by the system at a vertical resolution of 192 m and a temporal resolution of 60 min or 108,000 shots. A combination of electronic gating and mechanical chopping is used to define the lower altitude cutoff for the 95 and 5% channels. Integrating the high-latitude channel over 10 range gates to give a vertical resolution of 1.92 km and calibrating the relative density at 30 km altitude by radiosonde data taken that night by the Danish Meteorological Institute (DMI) 220 km north/northwest of the site results in the absolute atmospheric number density shown in Fig. 3(b).

The absolute number density is derived from the lidar profile using the expression

$$n(z)=n(z_{30\ \mathrm{km}})\ \frac{D(z)}{D(z_{30\ \mathrm{km}})}, \tag{7}$$

where

$$D(z)=\frac{z^2\hat{s}(z)}{C(\lambda)q^2(z,z_{\mathrm{ground}})R(z)} \tag{8}$$

is the relative density profile that is dependent on the system constant $C(\lambda)$, the atmospheric extinction from the ground to z, $q^2(z,z_{\mathrm{ground}})$, and the aerosol backscatter ratio $R(z)$. The normalization of the relative density in Eq. (6) essentially removes the dependency on the system constant as well as on aerosol contamination and atmospheric transmission below the normalization altitude of 30 km. Above the normalization altitude it is assumed that R is equal to one and that $q^2(z,z_{30\ \mathrm{km}})$, the extinction from the z altitude to the normalization altitude, is constant. The dashed curve in Fig. 3(b) represents the unfiltered estimate $n(z)$ of the density while the solid curve is the smoothed estimate $\hat{n}(z)$. The smoothed estimate is determined by applying the filter, described in Section 3 and in the appendix, to the high-altitude signal in Fig. 3(a) and estimating the relative density using Eq. (7). The prior signal estimate used in constructing the filter was determined from the hour of observations and the covariance variable γ was set to 3. The filter kernels used to smooth the 60-min profile are displayed in Fig. 10 in the appendix.

The error associated with the filtered number density is given in Fig. 3(c). In quantifying the error, the relative error $\sigma_{\hat{n}}(z)/\hat{n}(z)$ is typically used because it is this quantity that factors into the error analysis for the derived parameters. The inverse of the relative error provides the SNR. The relative error for $\hat{n}(z)$ follows from Russell and Morley[39] and is estimated here as

$$\frac{\hat{\sigma}_n(z)}{\hat{n}(z)}=\left\{\left[\frac{\sigma_n(z_{30\ \mathrm{km}})}{n(z_{30\ \mathrm{km}})}\right]^2+\left[\frac{\sigma_{\hat{s}}(z)}{\hat{s}(z)}\right]^2+\left[\frac{\sigma_{\hat{s}}(z_{30\ \mathrm{km}})}{\hat{s}(z_{30\ \mathrm{km}})}\right]^2\right\}^{1/2}, \tag{9}$$

where the estimate of the number density at 30 km, the filtered signal error at 30 km, and the filtered signal error at z are used in determining the total density error.

Figure 3(c) is a profile plot of percentage error determined from Eq. (9) for the filtered density profile shown in Fig. 3(b). Also shown are the percentage error profiles that would result using the normal sample error (dashed line), given by Eq. (1), and the Poisson error (solid line) for the unfiltered density profile. As discussed in Section 3, the difference between these two errors represents the error in the signal caused by variations in the scattering medium. Because the basis of the filter is to remove the Poisson counting fluctuations by smoothing while preserving the natural fluctuations of the medium, the filter error, shown in Fig. 3(c) and expressed in Eq. (24) in the appendix, will always be less than the Poisson error. The filter error will approach the Poisson error at low altitudes as the variance in the signal is strongly dominated by natural fluctuations $\sigma_s^2(z)$. At higher altitudes, more smoothing is applied by the filter as $\sigma_s^2(z)$ decreases. A constant filter function is used above about 55 km where $\sigma_s^2(z)$ becomes indeterminable and results in a factor of two reduction in percentage error as a result of the statistical Wiener filtering. It should be recognized at this point that the total variance in the density should include the variance of the scattering medium due to gravity waves, $\sigma_s^2(z)$, as it is not accounted for in the filter variance. For the data presented in Fig. 3, the density percentage error due to gravity waves was about 0.5% near 35 km. This uncertainty in the density due to gravity wave activity over the 1-hr integration period results in about a 1 K perturbation in temperature at 35 km.

4.2 *High-Background, Twilight Observations*

Because of the site's location north of the arctic circle, frequent observations are made during sustained periods of twilight. To reduce the solar background during these

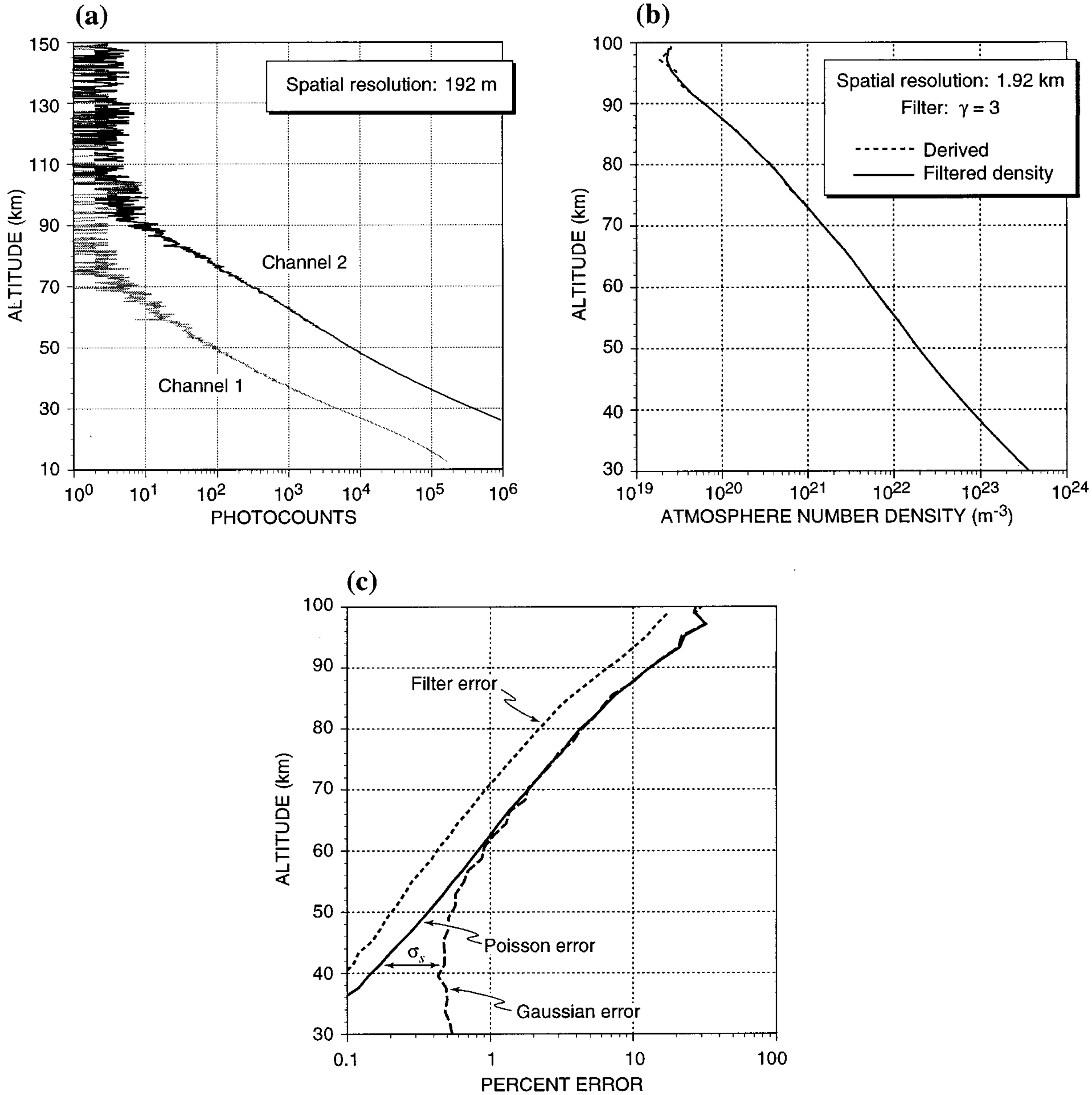

Fig. 3 Sample of lidar data taken during the night of April 10, 1996, integrated for 60 min or 108,000 shots with (a) raw signal counts from both channels; (b) comparison of filtered and nonfiltered derived atmospheric number density from the high-altitude channel with 1.92 km vertical resolution and $\gamma = 3$; and (c) percentage error for the number density shown in (b) using the filter estimate, Poisson estimate, and normal estimate.

times, we use a combination of optical elements including a narrowband filter, rotating half-wave plates and a polarizer in the receiver optics (see Fig. 1). It is well known that unpolarized light from the twilight sun is almost completely polarized when viewed at a 90 deg scattering angle. The degree of polarization at the 90 deg scattering angle is wavelength-dependent and, for the receiver wavelength of 532 nm, is nearly 90% vertically polarized.[40] Therefore, during these times, the background light observed from a vertically viewing lidar receiver will be highly polarized (multiple scattering and ground reflections will cause some depolarization). By incorporating a half-wave plate and polarizer into the receiver optics, we can, theoretically, reject 99% of the vertically polarized light and transmit 95% of the horizontally polarized light.[41] Once the background rejection is optimized, the linearly polarized laser pulses at 532 nm can be transmitted in the horizontal plane of polarization and scattered back to the receiver with little modification to its original polarization. It is important to note that synchronously rotating half-wave plates in the transmitter and receiver are necessary to maintain orthogonality between the polarization planes of the solar background and laser transmitter as the sun position changes.

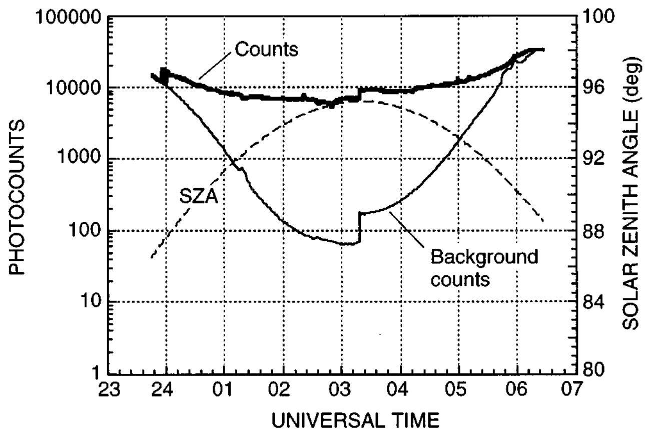

Fig. 4 High background observations illustrating the influence of the polarizer receiver configuration on the mean background counts and the raw lidar counts at 30 km as the solar zenith angle changes with time.

Polarization measurements of the background signal alone during twilight conditions resulted in a 75% reduction when the polarizer was placed in the optical path. The impact of the polarizer on the laser signal was tested during low background conditions (i.e., night). An illustration of the polarizer performance is shown in Fig. 4 for data taken on May 10, 1994. The display contains the mean background counts, signal counts at 30 km, and the change in solar zenith angle over the period of observations. For this experiment, the half-wave plate and polarizer were used at the beginning of observations and then removed at the peak solar zenith angle, leaving only the 532.0 nm filter with 1.0 nm bandwidth in the optical path. For this night, the presence of the polarizer resulted in a 25% reduction in laser signal and a 75% reduction in background. We have since improved the laser transmission through the polarizer to better than 10% reduction in laser light by fine tuning the polarization plane of the transmitted beam. Thus, the use of the polarizer improves lidar performance during twilight conditions by a factor of 3 to 4. The polarization technique alone becomes ineffective for solar zenith angles greater than 88 deg, partly due to the linear decrease in the degree of polarization with decreasing solar zenith angle, but mostly due to the exponential increase in the background intensity with decreasing solar zenith angle.

The other approach we use during these high background conditions is narrowband spectral filtering. Here, we use a Daystar filter consisting of a solid mica étalon and an interference filter, centered on 532.05 nm with a 0.08 nm bandwidth and approximately 25% transmission to limit the spectral passband of the system. Thayer et al.[42] present results comparing the polarization and narrowband filtering techniques used in the ARCLITE system based on solar zenith angle and signal relative error. They found that the time or solar zenith angle where the relative error of the two techniques cross is altitude-dependent. This is because of the different influences the two optical elements have on the laser signal and on the time-varying background signal. This effect can be explained by expressing the relative error in a signal-dominated regime as $1/[\langle s(z)\rangle]^{1/2}$, and the relative error in a noise-dominated regime as $\sqrt{\langle b\rangle}/\langle s(z)\rangle$. For solar zenith angles greater than about 95 deg, the lidar return signal is signal-dominated until about 70 km. Due to the greater transmission of the laser light by the combination of polarizer and broadband filter over the Daystar filter, the relative error is smaller than that associated with the Daystar filter during these times at all altitudes. As the solar background increases with decreasing solar zenith angle, the polarizer allows more background signal than the Daystar and, thus, experiences a much steeper increase in signal error with decreasing solar zenith angle. At 30 km altitude, the observations with the Daystar filter show better system performance than the observations with the polarizer for solar zenith angles less than about 85 deg. At higher altitudes this cross-over occurs at even greater solar zenith angles (87.5 deg for 40 km, 90.5 deg for 50 km, and 92 deg for 60 km) as the backscattered laser signal is weaker with height and, thus, influenced by the increasing background at greater solar zenith angles. Thus, for signal-dominated regimes the polarizer provides optimal system performance, while for background-dominated regimes the Daystar filter is best.

For middle atmosphere studies, this analysis helps determine the proper time to position the Daystar filter to improve system performance. For example, in detecting noctilucent clouds in the backscattered lidar signal during the arctic summer it is desirable to optimize performance at the 50 to 60 km altitude range as the backscattered signal from these clouds is equivalent to Rayleigh backscatter in this altitude range (see Ref. 32). Therefore, from Thayer et al.[42] it is shown to best insert the Daystar filter near 90 deg solar zenith angle or less providing better than 10% error in the signal at 50 km while becoming less accurate at lower altitudes where the loss can be afforded. In practice, we use the Daystar filter and the polarizer together to reap the benefits of both techniques with the signal requirements for the specific experiment determining when to insert the Daystar filter.

4.3 *Systematic Errors Due to Signal-Induced Noise*

Systematic errors, such as those discussed by Keckhut et al.,[6] can inhibit the capability of lidar systems beyond their statistical limitations. We have discussed the statistical errors and have accounted for many of the systematic errors discussed by Keckhut et al. but feel a more detailed look at the errors due to signal detection is required, particularly concerning the effect of signal-induced noise on the Rayleigh signal. In many lidar applications that use photon counting for signal detection it is important to consider the effects of nonlinear detector response, gain changes, noise pickup, and after-pulsing on the detected signal profile as these are systematic effects that can degrade system performance (Refs. 43 and 44 and references therein).

Detector linearity is generally assumed in that the output electrical signal of the PMT is linearly proportional to the input light intensity. However, during periods of high-intensity light pulses, the PMT response becomes nonlinear due to saturation effects causing the overlap of pulses (i.e., pulse pile-up). This may result in the false reduction or, in some cases, enhancement of the detected signal, as discussed by Donovan et al.[35] This can be primarily eliminated by using two photomultipliers to cover the dynamic range of the signal profile, as we have employed in the

ARCLITE system, but this effect is also dependent on the rise time of the PMT and on the discrimination-counting system. To test for linearity, one can use neutral density filters and compare the reduced signal profile to the normal signal file or, as in our case, use the low-altitude channel and ratio it to the high-altitude channel. For the overlapping ranges between the two signals of 30 to 50 km, we found the ratio to be constant with height indicating that the stronger signal in the high-altitude channel is not affecting the linearity in the signal.

Gain changes of the PMT are due to changes in the electric potential caused by the generated signal current or variations in the current drawn by the bias network. This can be minimized by using Zener diodes in the last few dynodes and by setting the discriminator voltage well below the signal pulse height. Environmental noise picked up by the coaxial cables is also an important systematic noise issue. We employ RG 223/U coaxial cable and have been able to keep noise levels to less than a few millivolts. Finally, it has also been suggested that a restricted photocathode area, like the 2.5 mm diameter photocathodes used in the ARCLITE system, while decreasing the dark current, might reduce noise due to Cerenkov radiation, which results from cosmic rays and the radioactive decay of isotopes in the input window of the PMT (Ref. 45).

After-pulsing or signal-induced noise produces a bias in the detected PMT signal induced by intense backscattered laser radiation causing a longlived nonlinear decay in the output signal. The probability of signal-induced noise generally increases with increasing voltage on the PMT and the overall dark current rises sharply increasing the variance of the dark current and therefore reducing system performance. In addition to the increased variance, the nonlinear decay is difficult to remove completely from the background and contaminates the signal. The impact of signal-induced noise on the detected signal varies depending on the atmospheric transmission at the time of the measurement and on system parameters such as laser-telescope alignment and laser power. The high-intensity, near-field backscattered laser light causing the signal-induced noise may be geometrically reduced by arranging the transmitter and receiver in a biaxial configuration. The biaxial ARCLITE system, with 1 m separation between laser and center of telescope, has a geometric overlap function equal to unity at about 2 km altitude for a 1.0 mrad field of view, reducing the intensity of the near-field return. Electronic gating of the PMTs is also employed in the ARCLITE system to reduce the impact of the low-altitude, high-intensity signal. The high-voltage gating circuit could also introduce unwanted noise in the detected signal, therefore, care should be taken when employing the gating circuit (e.g., Ref. 27). The electronic gating circuit, designed by EMI Thorn, gates the tube off by applying a 250 V negative bias on the first dynode of the PMT. When gated on, a high-voltage transient contaminates the first 1 to 2 km of the detected signal.

The combination of biaxial configuration and electronic gating reduces the effect of signal-induced noise but, as demonstrated by McGee et al.,[46] does not eliminate it completely. Figure 5 is an illustration of this very effect, comparing the raw photocounts recorded by the ARCLITE system using electronic gating with and without mechanical chopping. The raw photocounts were first recorded for 1 h using a mechanical chopper and are shown by the black line. The next hour of raw photocounts were recorded without mechanical chopping and are shown by the gray line. Electronic gating was used throughout the 2 h of measurements with the PMT gated on at an altitude of about 27 km. Obviously, the impact of mechanical chopping is quite dramatic between the two profiles above about 80 km. The higher background in the signal profile without chopping is attributed to signal-induced noise as the two signal profiles were created from data taken an hour prior to and an hour after local midnight, respectively, with no change in sky conditions. The mean background values for the two cases determined between the altitude of 110 and 140 km are 2.6 photocounts, 192 m, 1800 shots with chopping and 15.9 photocounts, 192 m, 1800 shots without chopping, or over a factor of 6 in background signal. In addition, the effects of signal-induced noise are not linear with height, as can be seen by the gradual slope observed in the background of the profile without chopping, causing a residual bias in the noise-subtracted signal. This residual bias is a systematic error that can significantly impact the high-altitude signal, and, as we show in the next section, can severely impact the Rayleigh temperature retrieval technique.

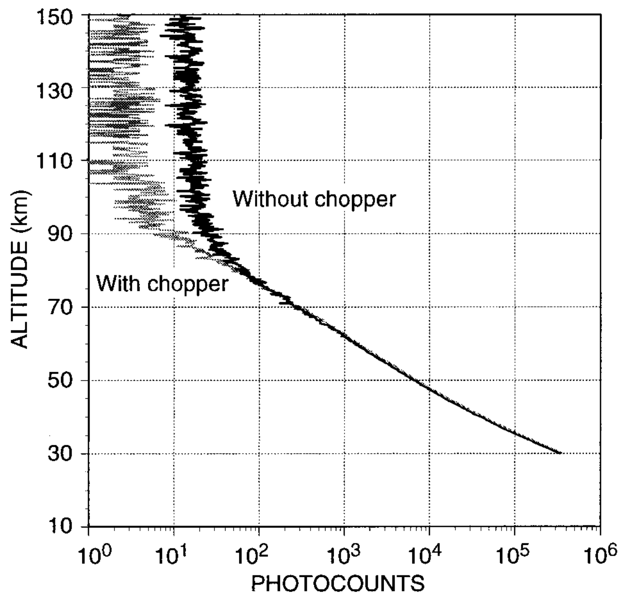

Fig. 5 Comparison between raw lidar signal integrated for 1 h using a mechanical chopper to block the low altitude return signal [same as Fig. 3(a)] versus raw lidar signal collected over the following hour without using a mechanical chopper.

5 Observations and Analysis

Lidar observations of the arctic middle atmosphere from the ARCLITE facility in Greenland began as a series of campaign efforts during the 1992 to 1993 winter with concentrated observing periods from November 30 to December 7, 1992, February 16 to 22, and April 6 to 13, 1993. More routine observations began in the summer of 1993 with an extensive data set obtained through the 1993 to 1994, 1994 to 1995, and 1995 to 1996 winter periods. Observations are made all year round with limitations on system performance depending on the time of year, as discussed in Section 4. Around the winter solstice, continuous observations of more than 24 h have been carried out. Observations using mechanical chopping began on April 10, 1996; care needs to be taken concerning signal-induced noise for measurements prior to this date, as shown in the previous section. Radiosonde measurements of temperature, pressure, wind, and humidity up to 30 km are recorded twice daily by the DMI from a station located 220 km north/northwest of the site; these measurements can be used to calibrate the lidar system, as was shown in Section 4. Recently, the DMI installed a balloon launch capability at Sondrestrom that operates on a campaign basis and allows direct comparisons between the lidar and various balloon payloads.[47]

5.1 *Temperature Analysis*

In addition to determining the atmospheric number density [as shown in Section 4 and Fig. 3(b)], it has been established that Rayleigh lidar systems, like ARCLITE, can provide precise middle atmosphere temperature profiles, assuming hydrostatic equilibrium and the ideal gas law, at high spatial resolution on a routine basis (e.g., Refs. 5, 39, and 48). The temperature retrieval technique we employ, described by Hauchecorne, and Chanin,[5] is where the temperature at height z_k in a layer thickness of Δz is given by

$$T(z)=\frac{g(z)\Delta z}{R\ \ln(1+X)}, \tag{10}$$

where $g(z)$ is the gravitational acceleration at altitude z, R is the gas constant for dry air, and X is expressed as

$$X=\frac{D'(z)g(z)\Delta z}{D'(z_n+\Delta z/2)RT_M(z_n+\Delta z/2)+\Sigma_{j=z+1}^{n}D'(j)g(j)\Delta z}, \tag{11}$$

where D' is the modified relative density given as

$$D'(z)=\frac{z^2\hat{s}(z)}{R(z)},\quad D'(j)=\frac{z^2\hat{s}(j)}{q^2(j,z)R(j)},$$
$$D'(z_n+\Delta z/2)=\frac{(z_n+\Delta z/2)^2\hat{s}(z_n+\Delta z/2)}{q^2(z_n+\Delta z/2,z)R(z_n+\Delta z/2)}. \tag{12}$$

The expression for X illustrates that the lidar-derived temperature profile is dependent only on the relative density profile when a model temperature, provided by MSIS-90 for example, is used at the top of the n'th layer or upper bound layer $T_m(z_n+\Delta z/2)$. As shown by Russell and Morley,[39] if a model pressure is used at the top of the n'th layer instead of temperature, the lidar-derived temperature profile is also dependent on the factor $n(z_{30\ \mathrm{km}})/D(z_{30\ \mathrm{km}})$, where $z_{30\ \mathrm{km}}$ is the index for the normalization altitude used to obtain the lidar-derived density profile. Thus, a temperature value used at the upper bound of the profile instead of pressure avoids the additional uncertainty in determining the density at the lower normalization altitude. The temperature relative error, employing propagation of error techniques, that we use in our analysis is written as

$$\frac{\sigma_T(z)}{T(z)}=\frac{X}{\ln(1+X)(1+X)}\left[(a)^2+(b)^2+(c)^2+(d)^2\right]^{1/2}, \tag{13}$$

where

$$a=\frac{\sigma_D(z)}{D'(z)},\quad b=\frac{\Sigma_{j=z+1}^{n}\sigma_D(j)g(j)\Delta z}{P'(z+\Delta z/2)},$$

$$c=\frac{\sigma_D(z_n+\Delta z/2)RT_{\mathrm{model}}(z_n+\Delta z/2)}{P'(z+\Delta z/2)},$$

$$d=\frac{\sigma_{T\mathrm{model}}(z_n+\Delta z/2)RD'(z_n+\Delta z/2)}{P'(z+\Delta z/2)},$$

with

$$\sigma_D(z)=z^2\sigma_{\hat{s}}(z),$$

$$P'(z+\Delta z/2)=D'(z_n+\Delta z/2)RT_M(z_n+\Delta z/2)+\sum_{j=z+1}^{n}D'(j)g(j)\Delta z.$$

Figure 6(a) is an example of lidar-derived temperature profiles from the high- and low-altitude channels and their associated errors determined from the same filtered data set as the number density shown in Fig. 3(b) with 60-min integration, 1.92 km vertical resolution, and $\gamma=3$. The MSIS-90 temperature profile for this day is also plotted and is given by the dashed line. The agreement in temperature between the two channels over the 30 to 50 km range attests to the PMT signal linearity of the high-altitude channel in this altitude range. A pervasive feature in this temperature profile, and many others determined from ARCLITE, is the presence of gravity waves. Further study concerning leewave sources of gravity waves at the site and variations in gravity wave activity determined from the lidar data is underway.

The contribution of each of the error terms a, b, c, and d in Eq. (13) is shown by Fig. 6(b) for the high-altitude temperature profile. The cumulative error estimate versus altitude for all four terms is shown by the short dashed line in the figure. The total temperature error is determined by applying the scaling factor $X/[\ln(1+X)(1+X)]$, which for this case was near 0.88, to the cumulative error presented in Fig. 6(b). The greatest contribution to the temperature error comes from the relative error of the signal a with the downward-integrated signal error b increasing its contribution as the integration is extended from the upper bound altitude of 84 km to lower altitudes. The error estimate associated with the upper bound parameters c and d using a model temperature error of 10 K, influences the temperature error within the first 10 km from the upper bound, as was also found by Hauchecorne and Chanin.[5] Larger errors in the upper bound temperature from the true temperature

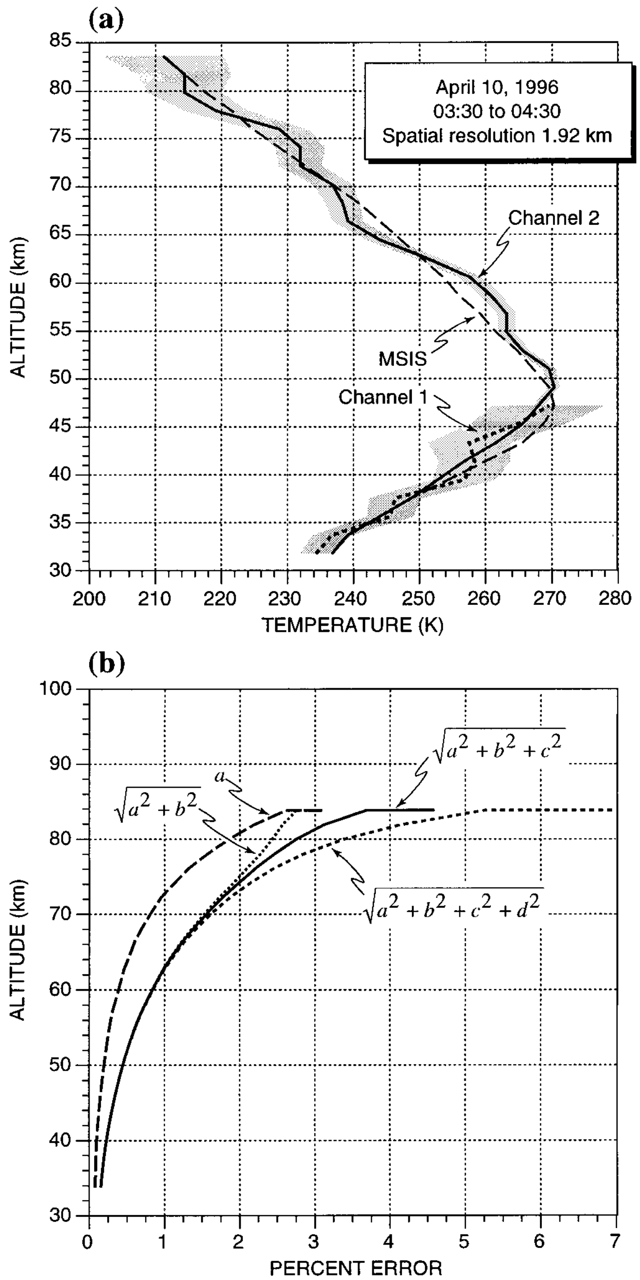

Fig. 6 (a) Lidar-derived temperature profile with one-sigma error for 60-min integration, 1.92 km vertical resolution, and $\gamma=3$ on April 10, 1996, with mechanical chopping of low-altitude signal. The profile was derived from the data presented in Fig. 3. The dashed line represents the MSIS-90 model temperature for that day. (b) Assessment of error contributions from the four terms given by Eq. (13) in the text.

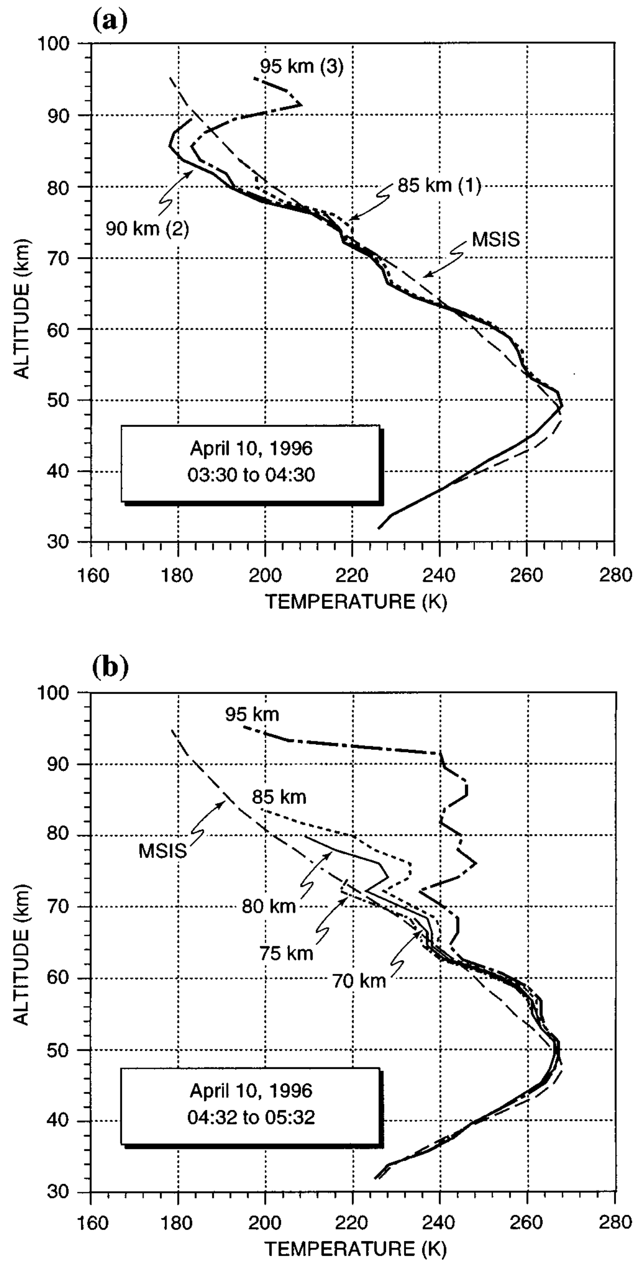

Fig. 7 (a) Same lidar-derived temperature profile as in Fig. 6 for three different starting altitudes of 84, 90, and 95 km. (b) Lidar-derived temperature profiles for five different starting altitudes (95, 85, 80, 75, and 70 km) with 60-min integration, 1.92 km vertical resolution, and $\gamma=3$ on April 10, 1996, without mechanical chopping of low-altitude signal.

would result in extending the influence of the model temperature to more than 10 km. Such a situation could occur when mesospheric inversion layers are present. The same is true if the error in the signal at the normalization height, quantified in term c, is unreasonably large.

Figure 7(a) illustrates the impact of the temperature estimate and the altitude chosen to begin the downward integration on the temperature retrieval technique. Here, the temperature profiles were determined, as discussed previously, for three different upper bound altitudes of 84 km (profile 1), 90 km (profile 2), and 95 km (profile 3). MSIS-90 was used to provide the upper bound temperature for each profile and is shown by the dashed line in the figure. The temperature error bars were left off of this plot for clarity. The three temperature profiles all converge at an altitude of about 76 km. Above this altitude, the influence of the model temperature at the 84 km altitude causes profile 1 to be warmer than the other two profiles. The higher altitude profiles remain close until about 82 km where again the model temperature at 90 km influences profile 2.

Profile 3 with the temperature fit at 95 km altitude shows two effects. One is the model temperature influence as recognized in the other profiles, and the other is the uncertainty of the relative density estimated from the lidar signal at 95 km. At 95 km, the density percentage error is near 15% [see Fig. 3(c)]. Using this estimate of density and the model temperature, the derived temperature at the top of the profile does not equal the MSIS-90 temperature like the other two profiles because of the increase in the relative density error. Due to the lidar signal becoming less representative at these heights because of noise, a false temperature inversion layer is formed. However, this effect only propagates about 10 km with the temperature estimate from profile 3 providing accurate estimates of temperature below about 84 km. As a result, in practice we set the altitude of the upper bound to be constrained to a signal percentage error below 15%, which is typically 10 km above the altitude of interest.

The temperature errors presented in Fig. 6(b) do not include the systematic errors discussed in the previous section. As we have shown in Fig. 6(a), PMT linearity at the lower altitudes of the temperature profile is not a cause of error as the temperatures derived from both channels are very similar. The effect of signal-induced noise, however, does impact the signal profile at high altitudes and must be carefully considered for data sets not using mechanical chopping. An illustration of the impact on the temperature analysis is shown in Fig. 7(b), where temperature profiles without chopping are compared for different starting heights. The temperature profiles in Fig. 7(b) correspond with the signal profile without mechanical chopping presented in Fig. 5. The impact of the signal-induced noise on the lidar signal is quite apparent in the temperature analysis. The higher the altitude used to fit the data the greater influence the signal-induced noise has on the temperature profile, with the 95 km fit influencing the downward temperature retrieval until an altitude of about 62 km. As the starting altitude is lowered, the influence becomes less and we begin to experience the same model temperature effects as illustrated in Fig. 7(a). Below about 75 km, the impact of signal-induced noise appears no longer to be significant as the temperature profile agrees reasonably well with the temperature profile shown in Fig. 7(a). Also, it is at and below this altitude that the signal profiles for the two cases shown in Fig. 5 converge.

It is clear from this analysis that signal-induced noise can have a profound impact on the determination of the atmospheric number density and temperature from the Rayleigh signal and on the overall performance of the lidar system. McGee et al.[46] describe approaches to try to remove the bias caused by signal-induced noise to improve their DIAL ozone measurements using an exponential fit to the background. However, uncertainty as to the choice of altitude to start the exponential fit and variability of signal-induced noise over different observing periods made the fit difficult to standardize. At present, we are limiting our temperature analysis to altitudes below the 2% signal percentage error level for lidar data taken without mechanical chopping. We will be pursuing approaches to try and improve the temperature analysis for these data contaminated with signal-induced noise in the near future.

5.2 *Aerosol Analysis*

The temperature and molecular density retrieval techniques discussed in the previous section are in error if aerosols are present in the lidar signal. This would be equivalent to the backscatter ratio $R(z)$ exceeding the assumed value of 1 and the extinction no longer being independent of height. This contamination places a lower altitude limit, assumed 30 km, for accurately determining the temperature and density, although the presence of noctilucent clouds near 83 km would also contaminate the upper altitude retrieval. The contribution of aerosols to the backscattered lidar signal can be determined from the single-wavelength measurement by evaluating the lidar backscattering ratio, defined as

$$R(z)=\frac{\beta_\pi^M(z)+\beta_\pi^A(z)}{\beta_\pi^M(z)},$$

where $\beta_\pi^M(z)$ is the molecular volume backscatter coefficient, and $\beta_\pi^A(z)$ is the aerosol volume backscatter coefficient. The backscatter ratio is determined from the second, low-altitude, photon-counting channel by normalizing the signal to an altitude void of aerosols and where the signal, transmission, and molecular volume backscattering coefficients are sufficiently well determined.

Lidar backscatter ratios (normalized at 30 km) are illustrated in Fig. 8 in a 3-D format of time, altitude, and backscatter ratio. The altitude range is from 10 to 30 km with a sample of data taken for different periods covering the period from winter 1992 to winter 1994. The data are presented in this format to illustrate the presence of Mt. Pinatubo aerosols above the site and the gradual reduction in aerosol concentration over the 2-yr period. The figure also illustrates the dynamic changes in the aerosol altitude distribution with time and verifies the assumption of $R(z)$ equal to one at 30 km in performing the temperature analysis. The position of the polar vortex with respect to Sondrestrom contributes to the dynamic distribution of the aerosols with time. For example, according to the European Centre for Medium-Range Weather Forecasts (ECMWF), on December 4, 1992, Sondrestrom was located outside of the polar vortex[47] and aerosols extended to altitudes in excess of 27 km. During February 18, 1993, the facility was located inside the vortex and the aerosol data were concentrated in the lower stratosphere, presumably due to downward transport of aerosols inside the vortex.

During the 1995 to 1996 winter, polar stratospheric clouds (PSCs) were detected by the lidar system on a number of occasions. Values for the PSC backscatter ratio were typically less than 10 with the clouds limited to altitudes below 25 km and quite often multilayered. However, on the morning of February 19, 1996, a PSC was detected with backscatter ratios in excess of 300. This event is shown in Fig. 9(a), where the backscatter ratio was calculated from the signal measured by the low-altitude channel and displayed in altitude versus universal time. Each profile represents 2 min of integration and a vertical resolution of 192 m. Profiles were excluded when the signal percentage error at the upper altitude, 26 km in this case, exceeded 12%. The variation in signal was caused by intermittent tropospheric cloud cover. Irrespective of the tropospheric clouds, the characteristics of the PSC can be seen throughout the observation period with unusually high backscatter ratios

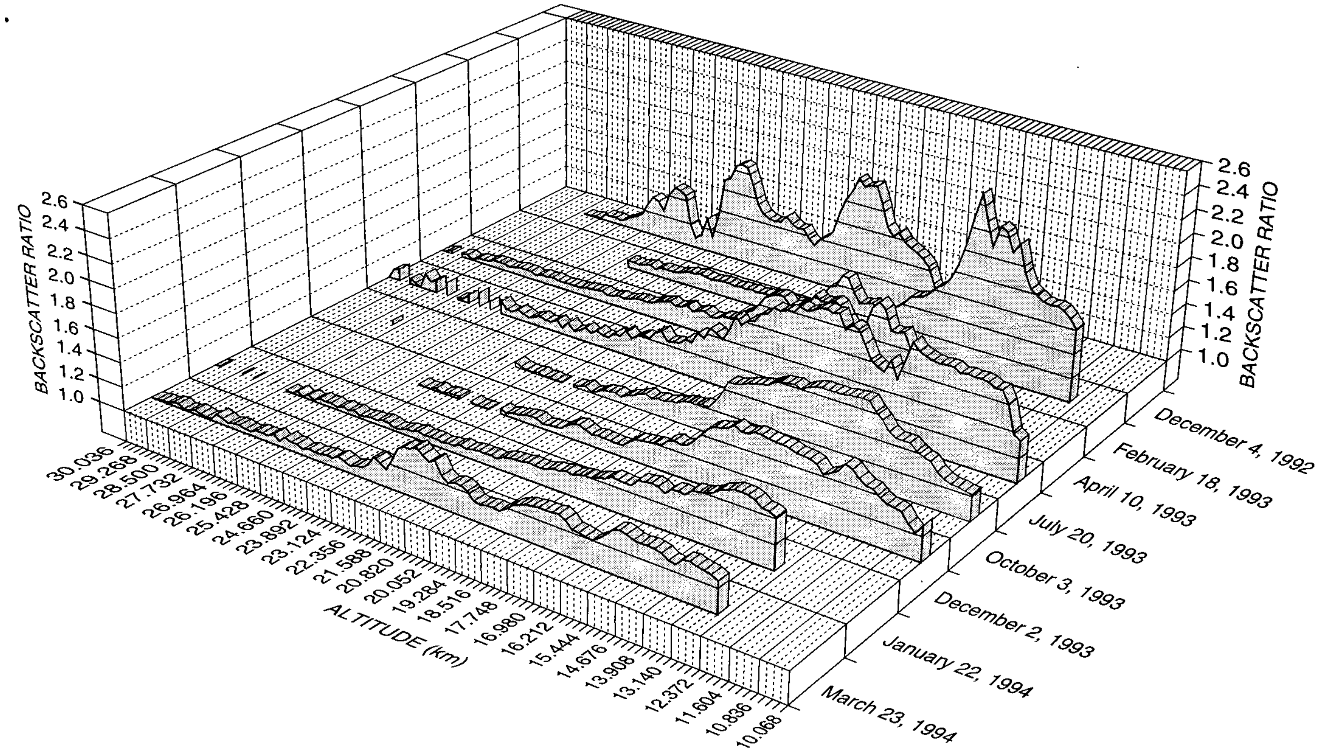

Fig. 8 Three-dimensional display of sample backscatter ratio profiles covering a 2 yr observation period. The truncation of the low-altitude data is not real but due to electronic gating of the signal at and below that altitude. The lines on the data profiles are the backscatter ratio values based on the *z* axis scale.

and, at times, a thickness of near 2 km. These are most likely ice water PSCs given the high backscatter ratio and the recorded cold lower stratospheric temperatures of 180 K from the radiosonde measurements by the DMI. Further analysis of this data set is underway.

Over the past 3-yr of summer observations, the ARCLITE Rayleigh lidar has also detected the existence of unique noctilucent clouds (NLCs). The presence and formation of these clouds are very different from PSCs as they occur only in the summer time and in a very different altitude region, averaging near 83 km in the upper mesosphere. A detailed discussion of the 1994 summer observations of NLCs by ARCLITE is given by Thayer et al.[32] Seventeen nights of NLC observations have now been recorded by the ARCLITE system. These clouds consist of ice water with particle sizes of less than 100 nm and can have backscatter ratios in the hundreds. Figure 9(b) is an illustration of a recent NLC event that occurred on August 8, 1996, plotted in terms of the backscatter ratio. The backscatter ratio was calculated from the signal recorded by the high-altitude channel and is displayed in an altitude versus Universal Time plot. The backscatter signal from the clouds presented in Fig. 9(b) is, on average, equivalent to the Rayleigh backscatter signal near 55 km. The presence of these clouds provides clues as to the basic state of the upper summer mesosphere and the detection provides detailed information on the basic characteristics of these clouds as well as elucidating the cloud's microphysics, as discussed by Hecht et al.[49]

6 Conclusions

We have presented a detailed description of a new Rayleigh lidar facility in Greenland called the ARCLITE facility. We have also described our data analysis procedures and highlighted some of the geophysical parameters derivable from the measurement. The limited amount of high-latitude observations of the middle atmosphere currently available emphasizes the importance and utility of a permanent lidar system in Greenland to investigate properly the phenomenological, synoptic, and climatological properties of the arctic middle atmosphere on a continuous, long-term basis. The unique location of the Sondrestrom facility enables middle atmosphere investigations concerned with temperature, gravity wave propagation, stratospheric aerosols, auroral influences, noctilucent and polar stratospheric clouds, polar vortex dynamics, and stratospheric warming-mesospheric cooling events. In addition, the impressive assemblage of optical and rf instrumentation at the site invites many new cooperative, multi-instrumented experiments to be carried out with the lidar. These investigations will benefit from this system's capability to determine accurately the temperature, density, wave characteristics, aerosols, and clouds contained within the middle atmosphere.

7 Appendix

In this appendix we outline the derivation of the filter used to process the lidar profiles $x(z)$ to get smoothed estimates of relative density and its covariance. The approach used is

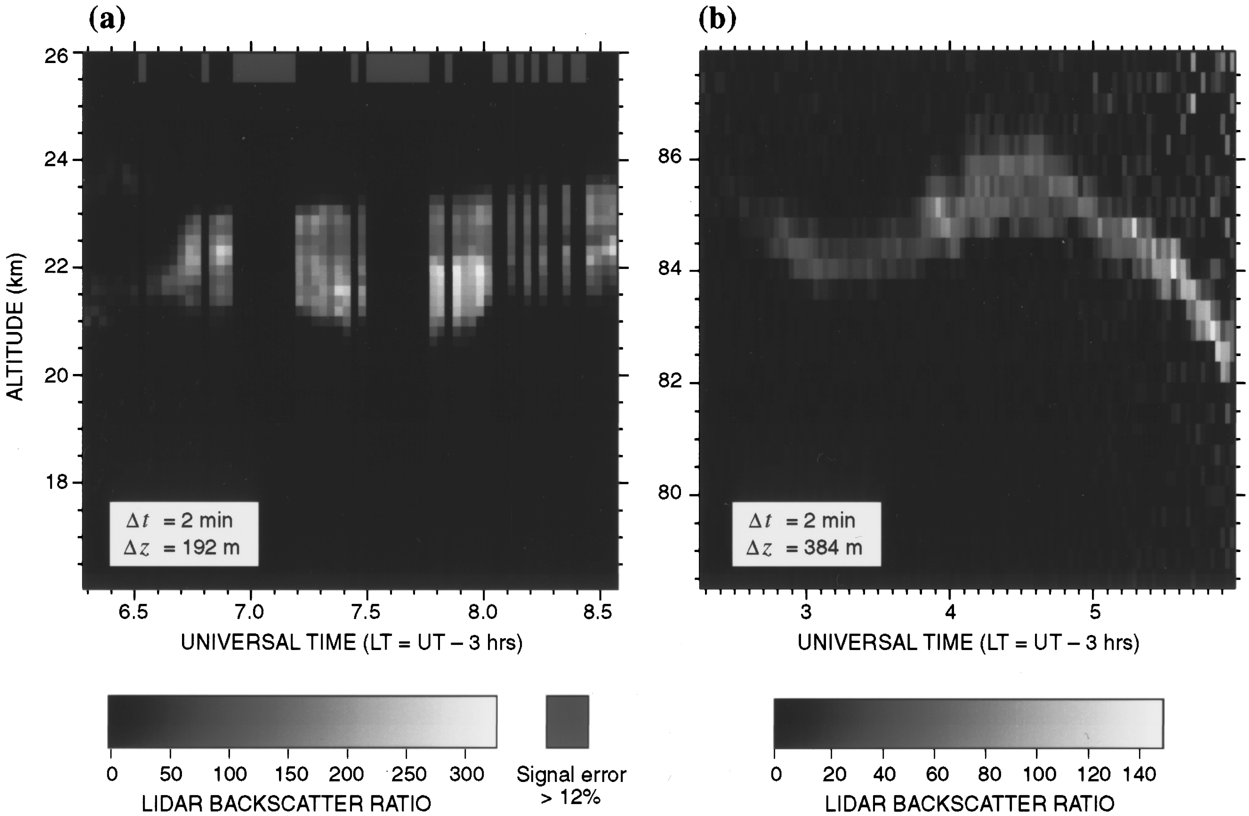

Fig. 9 (a) Backscatter ratio measurements by ARCLITE on February 19, 1996, of a polar stratospheric cloud with extremely high backscatter properties. Profiles with a signal percentage error of greater than 12% were excluded. (b) Backscatter ratio measurements by ARCLITE on August 8, 1996, of unique noctilucent clouds.

to construct Bayesian maximum *a posteriori* (MAP) estimators for the signal component $s(z)$ of the lidar data using approximate probability density models for the data $x(z)$ and prior estimates of the mean and covariance of the signal $s(z)$.

Letting $x(z)$ denote the received counts over a 1-min (or longer) integration time, we have

$$x(z)=s(z)+b, \tag{14}$$

where

$$s(z)\propto\frac{\rho_r(z)}{z^2} \tag{15}$$

represents the random signal component of the data in terms of the relative atmospheric density $\rho_r(k)$ and gate height z. We characterize the process $s(z)$ by its mean $\langle s(z)\rangle$ and range gate covariance Λ_s having components

$$\Lambda_s(z,z')\equiv E[s(z)-\langle s(z)\rangle][s(z')-\langle s(z')\rangle], \tag{16}$$

with E denoting statistical expectation. The covariance Λ_s models the fluctuation and correlation structure of the random density in range. The range gate covariance $\Lambda_s(z,z')$ is modeled and computed as

$$\Lambda_s(z,z')=\sigma_s(z)\sigma_s(z')\exp\left[-\frac{(z-z')^2}{\gamma(z)^2}\right], \tag{17}$$

using Eq. (4) and an estimate for the gate correlation scale parameter $\gamma(z)$. The values for $\gamma(z)$ are user-dependent and determine the degree of smoothing with altitude. The estimates of $\langle s(z)\rangle$ and $\sigma_s^2(z)$ are generated from the data as described in Section 3.

The filter used to produce smoothed estimates of $s(z)$ has the form

$$\hat{s}(z)=\sum_{z'=1}^{N}[\delta_{zz'}-H(z,z')]\langle s(z')\rangle+\sum_{z'=1}^{N}H(z,z')\times[x(z')-\langle b\rangle], \tag{18}$$

with the smoothing kernel H given as

$$H\equiv\Lambda_s(\Lambda_s+\Lambda_{x|s})^{-1}, \tag{19}$$

where

$$\Lambda_{x|s}=(\langle s(z)\rangle+\langle b\rangle)\delta_{zz'}, \tag{20}$$

and

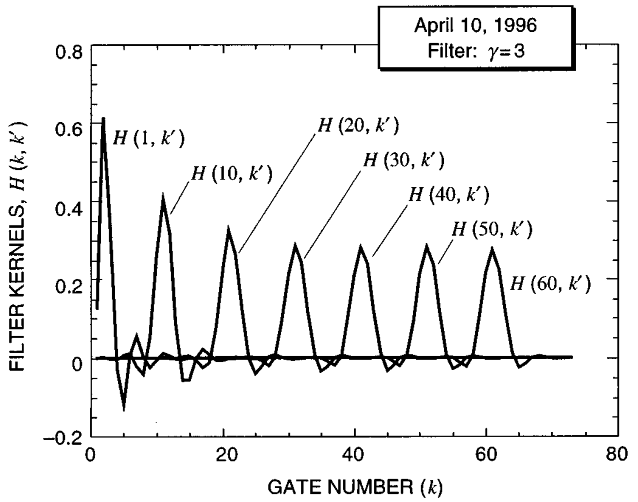

Fig. 10 Plot of filter kernels $H(k,k')$ determined from the April 10, 1996, data for $\gamma=3$ used in analyzing the data presented in Figs. 3 and 6. The abscissa is in units of gate number k starting at an altitude of 30.42 km with an increment of 0.96 km.

$$\delta_{zz'}=\begin{cases}1, & z=z',\\ 0, & z\neq z'.\end{cases} \tag{21}$$

The second term in Eq. (18) has the form of a range-gate-dependent convolution of the data $x(k)$ after mean background subtraction $\langle b\rangle$ by a kernel H constructed to produce relatively little smoothing at low altitude (high SNR) gates, and progressively more smoothing at higher gates. It can be interpreted as a Wiener filter in range gate space. The first term in Eq. (18) represents a filtered version of the prior signal $\langle s(z)\rangle$. In practice, this term becomes more important at high range gates in comparison with the Wiener filter component.

A plot of the smoothing kernel H at select range gates k for the data presented in Fig. 3 is shown in Fig. 10. Neglecting the effect of range gate covariance, the amplitude of the smoothing kernel is

$$H(z,z)=\frac{\sigma_s^2(z)}{\sigma_s^2(z)+\langle x(z)\rangle}=\frac{[\sigma_s^2(z)]/\langle x(z)\rangle}{1+[\sigma_s^2(z)]/\langle x(z)\rangle}. \tag{22}$$

The filter amplitude decreases with height due to the variance of the mean signal becoming more significant than the variance of the medium, as can be confirmed by Eq. (22). This decrease in amplitude results in a stronger influence of the prior estimated signal $\langle s(z)\rangle$, at higher range gates. The spread or range gate smoothing by the filter is determined by the gate covariance structure described by Eq. (17). The greater smoothing with altitude is a result of the weak correlation between gates at these higher gates.

The covariance of $\hat{s}(z)$ is given by

$$\begin{aligned}\Lambda_{\hat{s}}(z,z')&\equiv E[\hat{s}(z)-s(z)][\hat{s}(z')-s(z')]\\ &=\sum_{z''=1}^{N}[\delta_{zz''}-H(z,z'')]\Lambda_s(z'',z').\end{aligned} \tag{23}$$

Again, neglecting any range gate correlation, the variance of the smoothed estimate is given as

$$\sigma_{\hat{s}}^2(z)=\frac{\langle x(z)\rangle\sigma_s^2(z)}{\sigma_s^2(z)+\langle x(z)\rangle}=\frac{\langle x(z)\rangle}{1+\langle x(z)\rangle/\sigma_s^2(z)}. \tag{24}$$

Acknowledgments

This program was supported by the National Science Foundation Coupling of Energetics and Dynamics of Atmospheric Regions (CEDAR) program under the cooperative agreement, ATM-9317167. We would like to thank the Sondrestrom site crew and the support provided by the Danish Meteorological Institute.

References

1. G. E. Thomas, ''Is the polar mesosphere the miner's canary of global change?'' *Adv. Space Res.* **18**(13), 149–158 (1996).
2. R. P. Turco, O. B. Toon, and P. Hamill, ''Heterogeneous physicochemistry of the polar ozone hole,'' *J. Geophys. Res.* **94**(D14), 16493–16510 (1989).
3. R. S. Lindzen, ''Turbulence and stress owing to gravity wave and tidal breakdown,'' *J. Geophys. Res.* **86**(C10), 9707–9714 (1981).
4. M. E. McIntyre, ''How well do we understand the dynamics of strospheric warmings?'' *J. Meteor. Soc. Jpn.* **60**, 37–65 (1982).
5. A. Hauchecorne and M. L. Chanin, ''Density and temperature profiles obtained by lidar between 35 and 70 km,'' *Geophys. Res. Lett.* **7**(8), 565–568 (1980).
6. P. Keckhut, A. Hauchecorne, and M. L. Chanin, ''A critical review of the database acquired for the long-term surveillance of the middle atmosphere by the French Rayleigh lidars,'' *J. Atmos. Oceanic Tech.* **10**, 850–867 (1993).
7. J. A. Whiteway and A. I. Carswell, ''Rayleigh lidar observations of thermal structure and gravity wave activity in the high arctic during a stratospheric warming,'' *J. Atmos. Sci.* **51**, 3122–3136 (1994).
8. A. Hauchecorne, M. L. Chanin, and R. Wilson, ''Mesospheric temperature inversion and gravity wave breaking,'' *Geophys. Res. Lett.* **14**, 933–936 (1987).
9. J. W. Meriwether, P. D. Dao, R. T. McNutt, W. Klemetti, W. Moskowitz, and G. Davidson, ''Rayleigh lidar observations of mesosphere temperature structure,'' *J. Geophys. Res.* **99**(D8), 16973–16987 (1994).
10. J. A. Whiteway, A. I. Carswell, and W. E. Ward, ''Mesospheric temperature inversions with overlying nearly adiabatic lapse rate: an indication of a well-mixed turbulent layer,'' *Geophys. Res. Lett.* **22**, 1201–1294 (1995).
11. F. J. Schmidlin, ''Temperature inversions near 75 km,'' *Geophys. Res. Lett.* **3**, 173–176 (1976).
12. R. T. Clancy and D. W. Rusch. ''Climatology and trends of mesospheric (58-90 km) temperatures based upon 1982-1986 SME limb scattering profiles,'' *J. Geophys. Res.* **94**, 3377–3393 (1989).
13. J. A. Hauchecorne and A. Maillard, ''A 2-D dynamical model of mesospheric temperature inversions in winter,'' *Geophys. Res. Lett.* **17**, 2197–2200 (1990).
14. F.-J. Lübken, K.-H. Fricke, and M. Langer, ''Noctilucent clouds and the thermal structure near the arctic mesopause in summer,'' *J. Geophys. Res.* **101**(D5), 9489–9508 (1996).
15. U. von Zahn and W. Meyer, ''Mesopause temperatures in polar summer'', *J. Geophys. Res.* **94**, 14647–14651 (1989).
16. M.-L. Chanin and A. Hauchecorne, ''Lidar observation of gravity and tidal waves in the stratosphere and mesosphere,'' *J. Geophys. Res.* **86**(C10), 9715–9721 (1981).
17. T. Shibata, M. Kobuchi, and M. Maeda, ''Measurements of density and temperature profiles in the middle atmosphere with a XeF lidar,'' *Appl. Opt.* **25**, 685–688 (1986).
18. T. Shibata, S. Ichimori, T. Narikiyo, and M. Maeda, ''Spectral analysis of vertical temperature profiles observed by a lidar in the upper stratosphere and the lower mesosphere,'' *J. Meteor. Soc. Jpn.* **66**, 1001–1005 (1988).
19. C. S. Gardner, M. S. Miller, and C. H. Liu, ''Rayleigh lidar observations of gravity wave activity in the upper stratosphere at Urbana, Illinois,'' *J. Atmos. Sci.* **46**, 1838–1854 (1989).
20. R. Wilson, A. Hauchecorne, and M. L. Chanin, ''Gravity wave spectra in the middle atmosphere as observed by Rayleigh lidar,'' *Geophys. Res. Lett.* **17**, 1585–1588 (1990).
21. R. Wilson, M. L. Chanin, and A. Hauchecorne, ''Gravity waves in the middle atmosphere observed by Rayleigh lidar 1. Case studies,'' *J. Geophys. Res.* **96**(D3), 5153–5167 (1991).
22. R. Wilson, M. L. Chanin, and A. Hauchecorne, ''Gravity waves in the

middle atmosphere observed by Rayleigh lidar 2. Climatology,'' *J. Geophys. Res.* **96**(D3), 5169–5183 (1991).
23. N. J. Mitchell, L. Thomas, and A. K. P. Marsh, ''Lidar studies of stratospheric gravity waves: a comparison of analysis techniques,'' *Ann. Geophys.* **8**, 705–712 (1990).
24. N. J. Mitchell, L. Thomas, and A. K. P. Marsh, ''Lidar observations of long-period gravity waves in the stratosphere,'' *Ann. Geophys.* **9**, 588–596 (1991).
25. S. T. Gille, A. Hauchecorne, and M.-L. Chanin, ''Semidiurnal and diurnal tidal effects in the middle atmosphere as seen by Rayleigh lidar,'' *J. Geophys. Res.* **96**(D4), 7579–7587 (1991).
26. M. L. Chanin, A. Garnier, A. Hauchecorne, and J. Porteneuve, ''A Doppler lidar for measuring winds in the middle atmosphere,'' *Geophys. Res. Lett.* **16**(11), 1273–1276 (1989).
27. C. A. Tepley, ''Neutral winds of the middle atmosphere observed at Arecibo using a Doppler Rayleigh lidar,'' *J. Geophys. Res.* **99**(D12), 25,781–25,790 (1994).
28. G. Hansen, M. Serwazi, and U. von Zahn, ''First detection of a noctilucent cloud by lidar,'' *Geophys. Res. Lett.* **16**, 1445–1448 (1989).
29. L. Thomas, A. K. P. Marsh, D. P. Wareing, and M. A. Hassan, ''Lidar observations of ice crystals associated with noctilucent clouds at middle latitudes,'' *Geophys. Res. Lett.* **21**, 385–388 (1994).
30. G. Hansen and U. von Zahn, ''Simultaneous observations of noctilucent clouds and mesopause temperatures by lidar,'' *J. Geophys. Res.* **99**, 18989–18999 (1994).
31. M. Langer, K. P. Muller, and K. H. Fricke, ''Rayleigh lidar detection of aerosol echoes from noctilucent cloud altitudes at the arctic circle,'' *Geophys. Res. Lett.* **22**, 381–384 (1995).
32. J. P. Thayer, N. Nielsen, and J. Jacobsen, ''Noctilucent cloud observations over Greenland by a Rayleigh lidar,'' *Geophys. Res. Lett.* **22**(21), 2961–2964 (1995).
33. U. von Zahn, E. V. Thrane, and R. Skatteboe, ''The Alomar facility: status and outlook,'' in *Proc. 12th ESA Symp. on Rocket and Balloon Programmes & Related Research*, ESA SP-370, 379–385, Lillehammer, Norway, (1995).
34. A. I. Carswell, A. Ulitsky, and D. I. Wardle, ''Lidar measurements of the arctic stratosphere,'' *Proc. SPIE* **2049**, 9–23 (1993).
35. D. P. Donovan, J. A. Whiteway, and A. I. Carswell, ''Correction for nonlinear photon counting effects in lidar systems,'' *Appl. Opt.* **32**, 6742 (1993).
36. J. A. Whiteway and A. I. Carswell, ''Lidar observations of gravity wave activity in the upper stratosphere over Toronto,'' *J. Geophys. Res.* **100**(D7), 14113–14124 (1995).
37. R. E. Warren, ''Concentration estimation from differential absorption lidar using nonstationary Wiener filtering,'' *Appl. Opt.* **28**, 5047–5051 (1989).
38. C. S. Gardner, ''Sodium resonance fluorescence lidar applications in atmospheric science and astronomy,'' *Proc. IEEE* **77**, 408–418 (1989).
39. P. B. Russell and B. M. Morley, ''Orbiting lidar simulations. 2: Density, temperature, aerosol, and cloud measurements by a wavelength-combining technique,'' *Appl. Opt.* **21**, 1554–1563 (1982).
40. K. L. Coulson, *Polarization and Intensity of Light in the Atmosphere*, A. Deepak Publishing, Hampton, VA (1988).
41. J. W. Meriwether, R. Farley, R. T. McNutt, and P. D. Dao, ''Application of the Rayleigh lidar to observations of noctilucent clouds,'' J. Geophys. Res. **98**(D8), 14979–14989 (1993).
42. J. P. Thayer, N. B. Nielsen, R. B. Kerr, and J. Noto, ''Rayleigh lidar observations during arctic summer conditions,'' in *IEEE Proc. 1996 Int. Geoscience and Remote Sensing Symp.*, Vol. 1, pp. 686–690 (1996).
43. H. S. Lee, G. K. Schwemmer, C. L. Korb, M. Dombrowski, and C. Prasad, ''Gated photomultiplier response characterization for DIAL measurements,'' Appl. Opt. **29**, 3303–3315 (1990).
44. M. P. Bristow, D. H. Bundy, and A. G. Wright, ''Signal linearity, gain stability, and gating in photomultipliers: application to differential absorption lidars,'' *Appl. Opt.* **34**, 4437–4452 (1995).
45. M. L. Meade, ''Instrumentation aspects of photon counting applied to photometry,'' *J. Phys. E.* **14**, 909–918 (1981).
46. T. J. McGee, M. R. Gross, J. J. Butler, and P. E. Kimvilakani, ''Improved stratospheric ozone lidar,'' *Opt. Eng.* **34**, 1421–1430 (1995).
47. I. S. Mikkelsen, Private Communication, Danish Meteorological Institute (1994).
48. G. S. Kent and R. W. H. Wright, ''A review of laser radar measurements of atmospheric properties,'' *J. Atmos. Terr. Phys.* **32**, 917–943 (1970).
49. J. H. Hecht, J. P. Thayer, D. J. Gutierrez, and D. L. McKenzie, ''Multi-instrument zenith observations of noctilucent clouds over Greenland on July 30/31, 1995,'' *J. Geophys. Res.* **102**(D2), 1959–1970 (1997).

Jeffrey P. Thayer is a senior research physicist at the Geoscience and Engineering Center at SRI International in Menlo Park, California. His specialized professional competence is in high-latitude middle and upper atmospheric physics, aeronomy and ionospheric physics, neutral dynamics and electrodynamics, lidar instrumentation and analysis, passive optical instrumentation for upper atmospheric research, and incoherent-scatter radar for ionospheric studies. He received a BS in atmospheric science in 1984 from the State University of New York at Oneonta, an MS in atmospheric science in 1986 from the University of Michigan, and a PhD in atmospheric and space sciences in 1990 from the University of Michigan. He is a member of the American Geophysical Union, the Optical Society of America, and the American Meteorological Society.

Norman B. Nielsen is a senior research engineer at the Geoscience and Engineering Center at SRI International. He has designed and developed numerous ground-based and airborne lidar systems for both military and environmental programs. He has conducted extensive field work involving ultraviolet, visible, mid IR, and far IR lidar systems at worldwide locations. His current lidar interests involve frequency-agile differential absorption lidar systems, Raman systems, Rayleigh/Mie systems, and resonance systems.

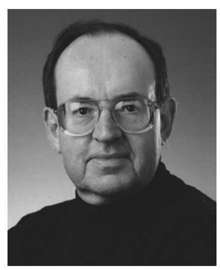

Russell E. Warren is a principal scientist at SRI International. His research interests include electro-optic model and statistical signal processing for lidar, imaging, and frequency modulation spectroscopic sensors. He holds a BA and an MS and received a PhD in physics in 1971 from the University of Iowa. Dr. Warren is a member of the American Statistical Association and IEEE.

Craig J. Heinselman is a senior research engineer in the Geoscience and Engineering Center at SRI International. His research interests include incoherent-scatter radar design and theory, radar pulse compression and signal processing techniques, ionospheric thin layer dynamics, and ionospheric plasma line measurements. He received a BS in engineering in 1979 from Harvey Mudd College and an MS in electrical engineering in 1996 from Stanford University, where he is presently pursuing a PhD in electrical engineering.

Jens Sohn is an engineer working for the Danish Meteorological Institute (DMI) at the Sondrestrom Incoherent-Scatter Radar Facility in Kangerlussuaq, Greenland. He provides engineering support for the radar, lidar, and ozone instrumentation at the site. He is responsible for the operation and maintenance of these instruments and contributes to the further development of the Greenland lidar system. He received a BS in electrical engineering in 1993 from the Engineering College of Aarhus, Denmark.